Topology-dependent hydrocarbon transformations in the methanol to hydrocarbons reaction studied by *operando* UV-Raman spectroscopy

Matteo Signorile[a], Daniel Rojo-Gama[b,c], Francesca Bonino[a], Pablo Beato[b*], Stian Svelle[c], Silvia Bordiga[a]*

[a] Department of Chemistry, NIS and INSTM Reference Centre, Università di Torino, Via G. Quarello 15, I-10135 and Via P. Giuria 7, I-10125, Turin, Italy

[b] Haldor Topsøe A/S, Haldor Topsøes Allé 1, 2800 Kgs. Lyngby, Denmark

[c] Center for Materials Science and Nanotechnology (SMN), Department of Chemistry, University of Oslo, P.O. Box 1033, Blindern, N-0315 Oslo, Norway

Keywords

MTH; Operando; UV-Raman; Deactivation; Zeolite; Heterogeneous catalysis

Abstract

The methanol to hydrocarbons (MTH) reaction represents a versatile, industrially viable alternative to crude-oil based processes for the production of chemicals and fuels. In the MTH reaction, the shape selectivity of acid zeolites is exploited to direct the synthesis towards the desired product. However, due to unavoidable side reactions occurring at process conditions, all MTH catalysts suffer deactivation due to coke formation. Though it is likely that some common characteristics for carbon formation exists for all zeolite topologies, it has been proposed that the differences in shape selectivity among the different catalysts will also influence the individual deactivation mechanisms. As deactivating species mostly aromatic compounds, such as highly methylated benzenes and/or polycyclic aromatic hydrocarbons (PAHs) have been discussed. In

some cases, these can further grow to extended carbon structures. Here, we have investigated the hydrocarbon reactivities and carbon formation for five topologically different zeolite catalysts through an *operando* UV-Raman approach, taking advantage of the high sensitivity of this technique towards aromatic and other carbonaceous species. The combination of the spectroscopic tool with activity measurements allowed us to obtain valuable details and some general trends on the deactivation paths during MTH. This approach made accessible unique insight on the complex chemistry proper of MTH by allowing the real time observation of hydrocarbon transformations proper of the peculiar topology of the catalyst, usually inaccessible by ex situ techniques.

1. Introduction

The conversion of methanol to hydrocarbons (MTH) represents an efficient non-petrochemical route for the production of chemicals and synthetic fuels from diverse carbon feedstocks such as natural gas, biomass or coal.[1, 2] The MTH reaction is an acid-catalysed process, heterogeneously promoted by strong acid materials: in the most common cases, the preferred catalysts are protonic zeolite. These are crystalline aluminosilicate materials with a three-dimensional framework containing interconnected channels and cages of nanometer sizes, characterized by a high porosity and surface area, strong Brønsted acidity and shape selective properties.[3-5] MTH over zeolites takes advantage of the superior selectivity toward desired ranges of products controlled by their microporous network features (i.e. their topology),[3] as well as from the closely monodispersed population of acid Brønsted sites (i.e. the active sites) in terms of acidity and local environment. Nevertheless, the reaction mechanism is complex and still not fully clarified in all its steps and it certainly involves several intermediate species, whose

speciation strongly depends on the degree of advancement of the reaction and on the specific zeolite catalyst. A schematic representation of the key process steps is given in Figure 1.

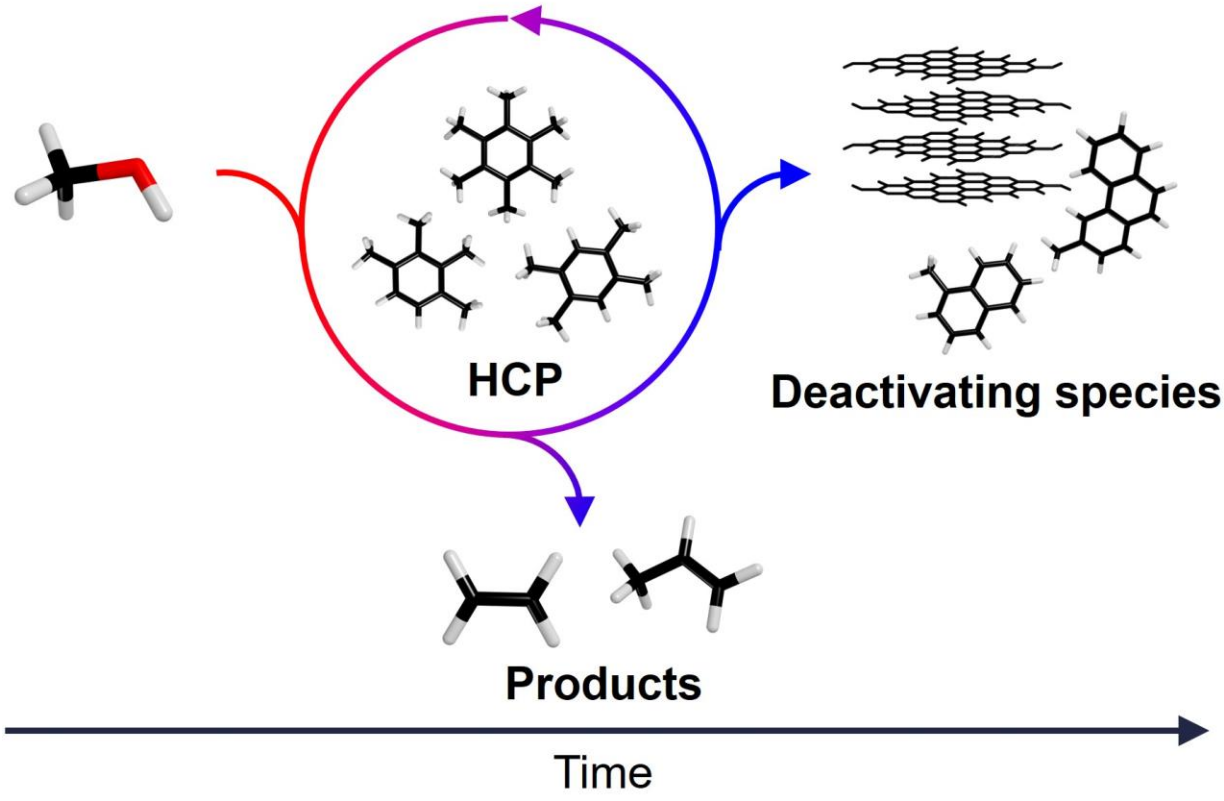

Figure 1. Schematic representation of the key steps in the MTH reaction mechanism.

In a very crude description, methanol is initially converted to olefins and aromatic species (mostly methylated benzenes, MBs), forming the so-called hydrocarbons pool (HCP). The HCP is a complex mixture of hydrocarbons (mostly aromatics) able to react with the strong acid Brønsted sites through continuous methylation and cracking processes. These repeated reactions generate a significant amount of light olefins, able to escape from the porous network (where are mostly located the active acid sites) and which are indeed the main products of MTH.[2, 6] Even though zeolites are the preferred catalysts for the MTH process, with increasing time on stream (TOS) the activity of the catalysts slowly decreases due to the formation of bulkier molecular

species or even carbonaceous deposits, that cannot leave the pores network and eventually completely deactivate the catalysts.[6]

The investigation of hydrocarbon transformations/deactivation mechanisms in MTH reaction has been carried out using very different approaches. On the one hand, the use of *ex situ* techniques on partially and/or completely deactivated samples has been largely applied.[7-11] However, since the deactivation of zeolites is a complex phenomenon influenced by different parameters such as reaction temperature,[6, 12] acid strength[13] or internal defects on the catalyst,[14, 15] the use of *operando* techniques is inherently more valuable because they provide insight into the formation and transformation of species during the reaction. Therefore, the MTH reaction has also been studied with *in situ* and *operando* techniques such as X-Ray diffraction,[16, 17] UV-Vis,[18, 19] IR[20] or EPR and INS spectroscopies,[21] among others.

Raman spectroscopy has proven to be a very valuable technique for the identification of the different allotropic forms of carbon.[22-25] It seems therefore obvious to choose Raman spectroscopy as a method to characterize the carbon species during the MTH reaction. However, Raman experiments on zeolites performed with conventional visible laser sources often fail because of the strong interference of competing emissive processes (e.g. fluorescence). Conversely, the use of UV excitation shifts the Raman signal to an energy range usually free from this type of side effects. Furthermore, many of the typical aromatic coke precursor molecules have electronic transitions in the UV range,[26-29] such that resonance conditions might be achieved. The resonance Raman effect represents a significant advantage, since it increases the sensitivity of the technique by orders of magnitude toward the resonant species. Nevertheless, the application of UV-Raman spectroscopy in the MTH reaction has been very limited because of possible sample damaging under the intense UV light which requires special

reactor systems.[30-34] Li and Stair were the first to apply UV-Raman spectroscopy to study the formation of coke over ZSM-5, SAPO-34 and USY during the conversion of methanol to olefins.[31, 32] The authors reported that for SAPO-34 the coke species are mainly of polyolefinic nature. In contrast, in ZSM-5 aromatic species seem to be the main constituents of coke, whereas for USY, polyaromatic or substituted aromatic species were identified as the dominant coke species. The differences in the nature of the deactivating species were related to the variation in pore size and structure for the three topologies.

In 2003, Chua and Stair performed an UV-Raman study after methanol dosing, applying for the first time a moving catalyst bed, in order to avoid laser damage of the organic coke precursors.[30] They suggested that for ZSM-5 polyolefinic compounds could cyclize to form cyclopentadienyl species which would be the key intermediates for the formation of aromatic and polyaromatic coke molecules. In 2018 An et al. presented a UV-Raman study on coke formation occurring during the methanol dehydration reaction over ZSM-5, i.e. a process similar to MTH but performed at lower temperatures (in the 150-200 °C in this specific work).[35] They showed as at low temperature "soft coke" species (identified as methylated benzenes, MBs, carbocations) are the most abundant and these are converted into "hard coke" (i.e. carbon and polycyclic aromatic hydrocarbons, PAHs) at higher temperature. They also identified a space-dependent distribution of the deactivating species in the reactor, as well-documented in the case of MTH (vide infra). Recently our group showed the potential of a newly developed fluid-bed micro-reactor in combination with UV-Raman to study hydrocarbon transformations in the MTH reaction.[33, 36-38] However, a systematic study of the MTH reaction over different zeolite topologies, applying *operando* UV-Raman spectroscopy is still missing.

It is important to mention that fluidization of the sample provides not only a tool to avoid sample damage, but also substantially effects the concentration of methanol and reaction products in the reactor. When ZSM-5 is used in MTH in a fixed-bed reactor, it is well established that deactivation occurs first at the top layers and then progressively proceeds toward the bottom.[7, 39-41] This behaviour, has also been described as a "burning cigar" type of evolution, and therefore the data will strongly depend on the sampling point, i.e. the laser focal point. Instead, fluidization makes the reaction occurring homogeneously, very much like in a continuously stirred tank reactor (CSTR) and thereby independent on the sampling position. While the latter effect is obviously beneficial for the purpose of characterization, care should be taken when trying to directly translate the observations to a fixed-bed reactor. Müller et al. compared the MTH reaction over ZSM-5 in a plug-flow reactor (PFR) with a CSTR at similar reaction conditions and showed that the CSTR leads to a dilution and a locally lower methanol concentration due to back-mixing with products.[42] This dilution leads to a much slower deactivation because the fast formation of methanol derived oxygenate species (e.g. formaldehyde), which they propose to be the precursor for aromatic hydrocarbons and eventually coke, are suppressed.

Here we present for the first time a real *operando* UV-Raman spectroscopic study of five different zeolite topologies during MTH reaction, by applying our in-house developed fluidized bed micro-reactor technology.[33] For the analysis of the complex data, a combination of the tools and insight of our previous studies is employed. UV-Raman spectra of representative PAHs have been recorded to be used as a reference database in combination with theoretical calculations,[29] facilitating the identification of MTH reaction intermediates. Further, we have used the same set

of catalysts, for which we previously analysed the deactivated materials by an *ex-situ* multi-technique approach.[8]

2. Experimental

Five catalysts with different topological properties were studied under operando conditions: Table 1 shows the list of the materials and their main topological and chemical features. Additional characterization data are provided in Table S1 (for full characterization details, see ref [8], as the materials used in this study are the same as those reported in our recent work). All the material (with the only exception of Beta) are characterized by low external surface area with respect to the overall value, as confirmed by the dominating fraction of the micropores volume over the total pores volume (i.e. most of the surface area is ascribable to the microporous network). Beta is the only catalyst exhibiting a significantly higher external surface area, compatibly with its low crystal size. Despite such morphological difference, the acidity of its Brønsted sites (evaluated from the red-shift of the IR band associated to the O–H stretching mode upon CO adsorption at 77K) is not largely different from ones of other catalysts, testifying the active sites shall have rather similar properties among the set of catalysts reported in this work. Furthermore, though enhanced morphologies (e.g. having multiple orders of porosity or peculiar crystal shapes) are known to improve the catalytic activity because of the better transport properties of these structures, however without deeply altering the reaction mechanism proper of a specific topology.[43-47]

Table 1. Details about the catalysts considered in this work

Sample	Topology[a]	Channel dimensionality	Larger ring size[b]	Si/Al	d_{max}^{diff} [cd]	d_{max}^{incl} [ce]
ZSM-5	MFI	3D	10	15	4.70	6.36
Beta	*BEA polymorph A	3D	12	17	5.95	6.68
Mordenite	MOR	1D	12	8	6.45	6.70
ZSM-22	TON	1D	10	47	5.11	5.71
SAPO-34	CHA	3D	8	11[f]	3.72[g]	7.37[g]

[a] conventional abbreviations from International Zeolite Association (IZA)[48]

[b] number of tetrahedral $[SiO_4]^{4-}$ units forming the larger ring of topology

[c] data from IZA website,[48] given in Å

[d] maximum kinetic diameter of species which can diffuse inside/outside the larger openings

[e] maximum kinetic diameter of species which can be included inside the pores network

[f] (Al+P)/ Si ratio

[g] data referred to the isostructural aluminosilicate Chabazite

UV-Raman spectra were collected with a Renishaw inVia Raman Microscope spectrometer, equipped with a 3600 lines mm^{-1} grating and Peltier cooled CCD detector. The excitation beam was focused on the sample through a 15× objective. The Rayleigh peak was removed by a dielectric edge filter. A Coherent MotoFred 300C frequency doubled Ar^+ laser, emitting at 244 nm, was used as excitation source.

Operando experiments were conducted exploiting the features of the modified Linkam CCR1000 microreactor previously reported by the authors.[33] In brief, the catalyst samples were pressed to pellets, crushed, and sieved to obtain a particle size of 150-300 μm. Fluidized-bed conditions were obtained through small periodic (50 Hz) backflow pulses, provided by a

membrane pump. About 20 mg of catalyst were loaded for each experiment. Before starting the reaction, each catalyst was oxidized at high temperature to remove the pre-existing carbonaceous residuals: samples were exposed to a 20 ml min^{-1} flow of pure O_2, then the temperature was raised up to 550 °C with a rate of 5 °C min^{-1}. After 30 min of oxidation at 550 °C, the temperature was decreased to 400 °C and, after a 5 min of purge with 20 ml min^{-1} He, the reaction was started by bubbling a 20 ml min^{-1} He flow through a methanol evaporator. The space velocity was kept to 2 $g_{MeOH}\ g_{cat}^{-1}\ h^{-1}$ by cooling the methanol down to 0 °C. On average, it was possible to follow the reaction for approximately 1 h. Such time frame was sampled by continuous spectra collection of ~5 min each, giving a reasonable balance among signal-to-noise ratio and time resolution. While collecting the Raman spectra, the qualitative composition of the flow outgoing the reactor has been continuously sampled with a Pfeiffer OmniStar GSD 320 O quadrupole mass spectrometer (MS). Due to the barely qualitative nature of the MS data, these are reported in the following "as such" (i.e. without further elaborations). For this reason, some relevant data from ref. 8, describing the catalytic behaviour of the materials in a rigorous way, are reported in Table S2. These have been derived through the Janssens model[49] and include the times on stream at which MeOH conversion drops to 50% ($t_{0.5}$, describing the absolute lifetime of each catalyst), the conversion capacities (R_0, which accounts for the overall productivity) and deactivation coefficients (*a*, accounting for the deactivation rate).

3. Results and discussion

We will start by presenting the obtained data for each sample first and then move to a comparative discussion, in order to highlight the differences among the samples. All the spectra reported in this work have been collected in the 1000-1800 cm^{-1} range, since the most important and univocal features of aromatic (MBs and PAHs), alkenes and extended carbon fall in this spectral region. In fact, lower frequencies modes are strongly affected by thermal effect, indeed their scattering intensities become closely nil.[50] Another potentially informative region includes Raman shift between 2700-3300 cm^{-1}, i.e. accounting for the typical C–H stretching modes. However, the latter intensities are much weaker than ones of ring modes proper of aromatic species, since resonance conditions (vide infra) selectively enhances such vibrations. Moreover, due to the fast spectra collection required in this work, the spectral quality (i.e. signal-to-noise ratio) achieved for C–H stretching modes might be insufficient for their fruitful assignment to specific species.

Most of the spectral assignments of this work concerning molecular species are based on ref [29]. The spectra of some additional relevant compounds are given in Figure S1 of ESI. Due to the complexity of hydrocarbons mixtures observed in this work, slight effect due to weak interaction of molecules with their surrounding environment (e.g. frequency shifts ascribed to their confinement in the microporous channels/cages of the zeolite catalysts) have been neglected during the assignment of the spectral features. Such approximation is however reasonable and it allows an unambiguous recognition of the bands pattern proper of a specific compound, according to the low net effect expected with respect to the spectra of the pure compounds ($|\Delta\nu| < 10$ cm^{-1}, i.e. comparable with the linewidth of the signals themselves).[29, 51]

The assignments related to bulk carbon phases refer to the work of Ferrari and Robertson:[23] in this regard, some key concepts are recalled hereafter, thus providing to the reader the necessary background for the data evaluation. The main peculiarity of UV Raman spectra of carbons is the substantial suppression of the so-called D band at around ~1400 cm^{-1} related to breathing motion of sp^2 aromatic rings. As a result, the D/G intensity ratio (the G band is ascribed to the stretching modes of pairs of sp^2 atoms in rings and chains, found around ~1600 cm^{-1}) is much lower compared to the Raman spectra of the same samples, when collected with visible excitation sources. In particular, with UV excitation the D band has maximum intensity when the carbon is rich in disordered sp^2 domains, e.g. as in an amorphous carbon. Another key point in the spectra interpretation is the strong dependency of the frequency shift of the G band on the relative sp^2/sp^3 contents: graphite like carbons exhibit the maximum closely below 1600 cm^{-1}, whereas increasing sp^3 contents lead to its blue-shift up to 1680 cm^{-1}. Furthermore, the eventual presence of C–C single bonds promotes the establishment of a further feature in the UV-Raman spectrum of carbons, labelled as T band, which usually falls in the 1000-1100 cm^{-1} range.

Despite the effort in building a representative library of reference compounds, the high chemical diversity in the deactivation products during the MTH reaction over different zeolite topologies does not ensure a rigorous assignment of all the spectral features on a purely experimental basis. Thus, additional simulation of Raman spectra through a DFT approach was applied in order to help the data interpretation. In particular, the effect of methylation on the Raman spectra of naphthalene, anthracene and phenanthrene was evaluated, avoiding the expensive and time-consuming measurements of a large set of additional reference molecules. The key results are given in Figure S2 of ESI, together with the calculations details.

Another important point to be addressed is the correct interpretation of intensities: these are in fact affected from both physical effects and instrumental aberrations. In the former category, the main actor is the resonance occurring with specific molecules: when resonance is achieved, linearity between the concentration of the specie and the intensity of its Raman signal is lost. Most of the aromatic species taking part to the reaction show their π-π^* (or n-π^*) transitions in the 200-300 nm window, thus allowing resonance enhancement to occur. However, even small variation in the excitation wavelength can have a large effect on the extent of the resonance (affecting both relative and absolute intensities).[52] This means that species whose electronic transitions fall closer to the excitation wavelength will in principle show a stronger signal enhancement compared to others. In the specific case of this work, the intensities associated to small PAHs like naphthalene, anthracene and phenanthrene with electronic transitions between 220-250 nm, will dominate over both single aromatic ring species (polymethylated benzenes, electronic transition at ~270 nm) and larger PAHs (electronic transition above 250 nm).[26-29, 53, 54] Analogously, we do not expect a relevant contribution from molecular species protonated upon their interaction with the Brønsted acid sites (i.e. carbocations), since their electronic transitions are expected at even longer wavelengths (> 300 nm).[28, 53, 54]

Noteworthy, the peculiar setup exploited in this work might introduce undesired instrumental aberrations. The most relevant to deal with, since the fluidized bed is used to avoid decomposition of deactivation products, is the instability in the focusing of the sample in time. This unavoidably leads to small variations in the absolute Raman intensities (for all species), making some type of normalization necessary (when comparing different samples with each other). A convenient normalization strategy would refer to a signal which is expected to be constant along the experiment, e.g. one related to the zeolitic framework (see as an example ref.

55). In this way, the relative variations of intensities would have quantitative meaning. Unfortunately, the Raman signals of the coke and coke precursor products are much more intense than the ones related to the zeolite ones (due to the resonance effect) [8], making a reliable normalization to the framework vibrations impossible already at short TOS. Consequently, the only viable solution has been to normalize the spectra to the most intense signal (*i.e.* the maximum of the 1600 cm^{-1} bands). Anyhow, since the main contribution to this signal is ascribable to bulk carbon, some semi-quantitative trends on molecular species can be obtained.

Finally, the spatial distribution of carbonaceous species with respect to the zeolite framework is hardly determinable on the basis of the bare UV Raman data. Still, taking in account the peculiar topology of each zeolite catalyst (i.e. shape, dimensionality and connectivity of its micropores), some general consideration can be inferred. Clearly, an extended carbon phase can only develop at the external surface of the zeolite particles, since the micropores are too narrow and prevents its growth herein for every topology considered in this work. Concerning molecular species, these can in principle be found both within the channels/cages of microporous network or adsorbed at the external surface of the particles. In the case accumulation of a molecular specie is observed, the former scenario should be logically more plausible, since the rather weak interactions among hydrocarbons and external surfaces could easily result in their easy desorption (whereas diffusion limitations of the molecules in the internal pore network reduce the desorption probability).

3.1. ZSM-5

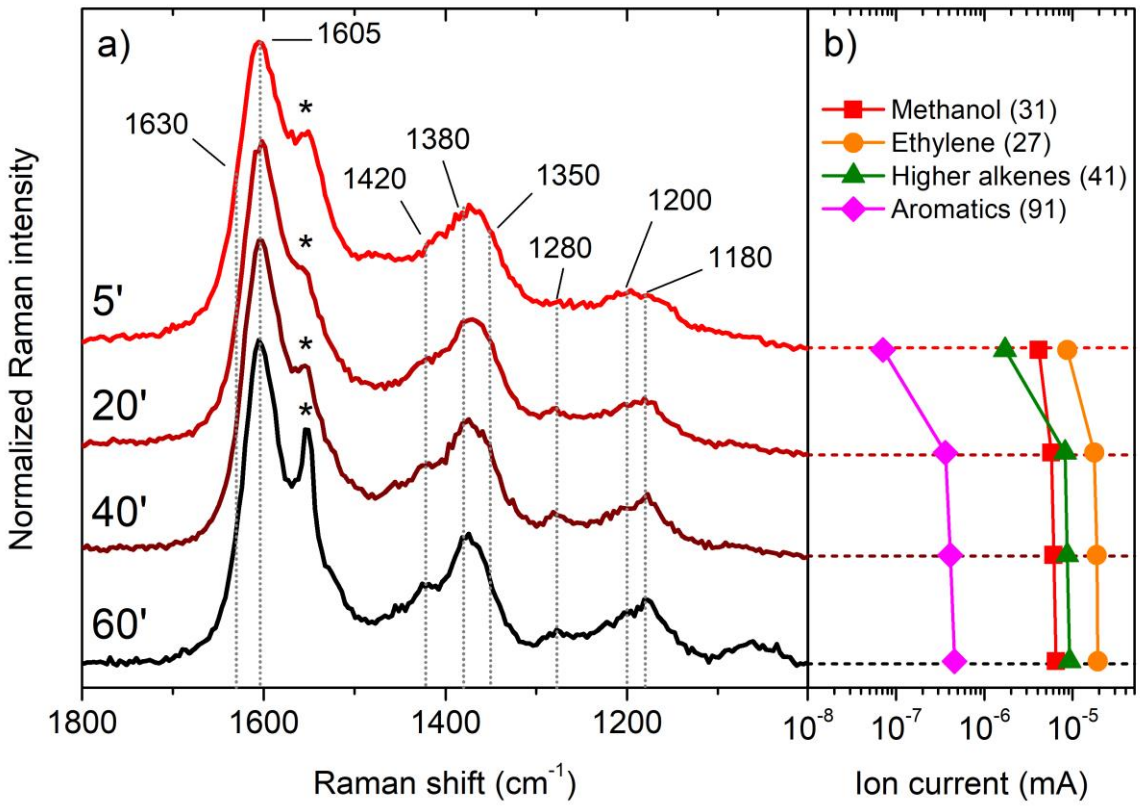

Figure 2. a) UV-Raman spectra of ZSM-5 collected at different TOS during the MTH reaction (400 °C, WHSV = 2 $g_{MeOH}\ g_{cat}^{-1}\ h^{-1}$). The asterisk (*) labels the contribution associated to atmospheric O_2. b) MS ion currents for methanol (red squares, m/z = 31), ethylene (orange circles, m/z = 27), higher alkenes (green triangles, m/z = 41) and aromatics (magenta diamond, m/z = 91), measured at TOS corresponding to the UV-Raman spectra reported above.

Figure 2a resumes the operando UV-Raman experiment on the ZSM-5 sample. Generally, the spectra are complex due to the superimposition of several chemical species. Nevertheless, it is possible to identify a number of maxima and shoulders related to specific molecular species. The most intense band is observed at 1605 cm^{-1} with a tail toward higher frequencies. The band maximum coincides with the ones for fluorene and biphenyl (see Figure S1b), which have also

been detected in dissolution-extraction experiments.[8] The tail extending to higher frequencies can be related to condensed aromatic molecules (i.e. PAHs), such as naphthalene, anthracene and phenanthrene (the latter also showing a second maximum at 1600 cm^{-1}, thus also contributing to the most intense peak). Furthermore, at 244 nm excitation, also bulk carbon presents its main fingerprint in this frequency region: the assessment of the carbon nature is not straightforward, because of the overlap of molecular features. However, according to the frequency and width of a possible underlying G band, this carbon is likely to be of amorphous type with high sp^3 content, as suggested by the modulation of the background around 1400 cm^{-1} (inferring the presence of a weak D band), and considering the growing background in the low frequency region, between 1000-1100 cm^{-1}, where the T peak is expected. Another feature, whose intensity randomly varies along the experiment, is a very sharp band centred at ~1550 cm^{-1} straightforwardly assigned to the O=O stretching of molecular oxygen.[56] This spurious contribution arises from the parasite Raman scattering of the atmospheric O_2 along the whole optical path of the instrument, thereby its absolute intensity is expected to be constant along experiment. Upon normalization to a sample mode, a high relative intensity of this band is indicative of a decreased contribution of the sample features to the overall Raman spectrum, e.g. caused by a poor focussing of the excitation beam over the specimen (as possibly occurring under fluidization conditions). Such randomized behaviour is fully decoupled from the catalyst topology, being of instrumental rather than chemical origin.

The assignments can be corroborated by the characteristic features in the 1400 cm^{-1} region, where the molecular fingerprints are easier distinguishable because of the minor contribution from extended carbonaceous species. The band has a peculiar shape with multiple maxima overlapping each other: the most intense along the whole set of spectra, centred at 1380 cm^{-1}, is

ascribed to naphthalene. The shoulder at 1350 cm^{-1} is related to heathen and progressively drops in intensity with respect to naphthalene as TOS increases. The 1420 cm^{-1} feature is not observed for any specific species considered as standard (see SI), however it falls between the main feature of anthracene (1400 cm^{-1}) and a secondary (but intense) peak of phenanthrene (1440 cm^{-1}). Possibly, the maxima at 1420 cm^{-1} originates from the convolution of these two species, as also suggested by its complex shape. Likewise, methylation of phenanthrene could give rise to Raman signals in that region (see Figure S2c). At advanced reaction times the overall spectral profile is rather broad, suggesting bulk carbon as the main coke component. However, some sharp maxima are still identified. As previously inferred by ex situ measurements,[8] this particular sample of ZSM-5 could follow a hybrid deactivation path, where bulk carbon and aromatic species coexist. This peculiar behaviour can be justified by the maximum kinetic diameter for molecules which can be included in the channels intersection, much larger than the size of species allowed to out-diffuse from the pores opening (see Table 1).

The precise assignment of the lower frequency region is not straightforward, as all the considered molecules possess vibrational modes around 1200 cm^{-1}. Furthermore, this spectral region is strongly affected by the methylation of molecules (see Figure S2). Noticeably, a time evolution is observed, as a component at 1180 cm^{-1} steadily increases with respect to another feature at 1200 cm^{-1} at increasing TOS. Interestingly, also a component at 1280 cm^{-1} shows up at longer TOS: this is likely to be related to the presence of polymethylated benzenes (PMBs) i.e. tetra- and hexa-methyl-benzene, which have their most intense vibrational Raman modes between 1200 and 1300 cm^{-1} (see Figure S1a and ref. [57-61]). The proposed assignments are in good agreement with the outcomes from Chua and Stair,[30] who reported a prevalence of

(poly)aromatic moieties in the retained species forming upon MTH reaction at high temperature (360 °C in their report).

The online mass spectra collected during the Raman experiments show that the ZSM-5 catalyst is still fully converting methanol after 60 min of reaction (see Figure 1b and Figure S3a for the full MS chart), in line with the catalytic descriptors given in Table S2 (showing its extended lifetime, high productivity and low deactivation rate). As expected, ZSM-5 produces both olefins and aromatics. However, it has been impossible to run longer *operando* experiments until methanol breakthrough and eventually complete deactivation, due to problems with the fluidization of the sample for extended timeframes.

3.2. Beta

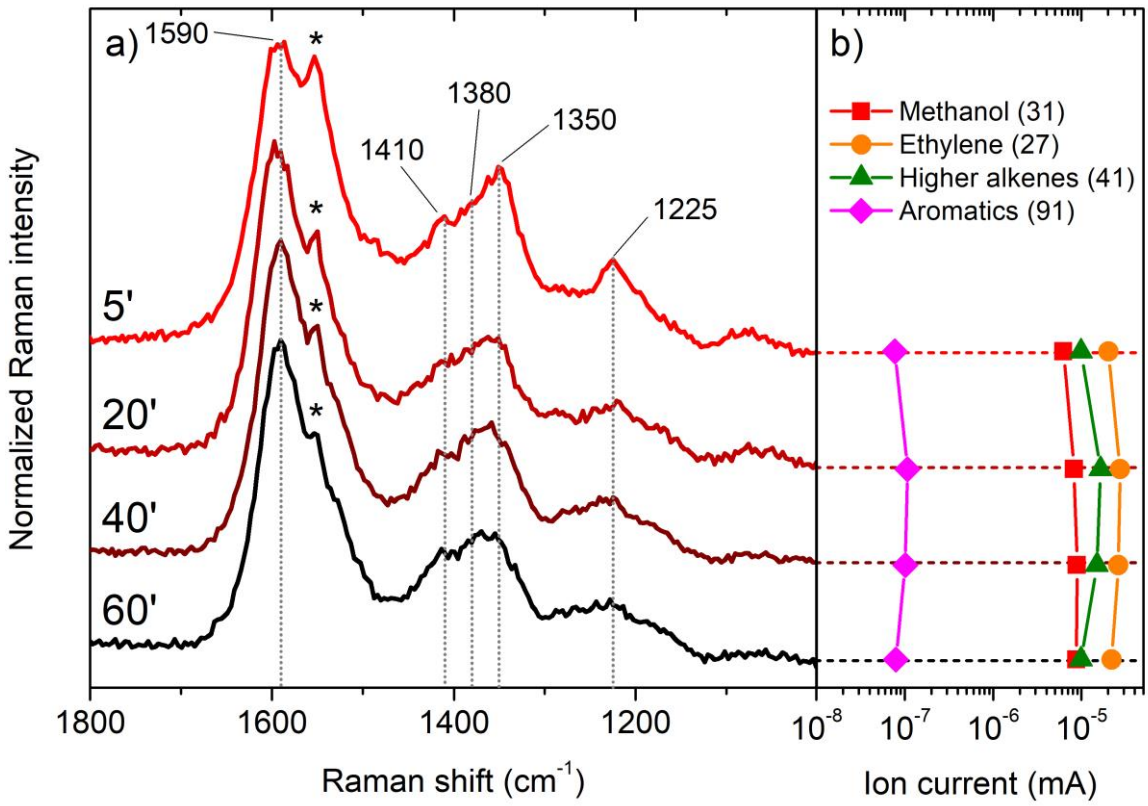

Figure 3. a) UV-Raman spectra of Beta collected at different TOS during the MTH reaction (400 °C, WHSV = 2 $g_{MeOH}\ g_{cat}^{-1}\ h^{-1}$). The asterisk (*) labels the contribution associated to atmospheric O_2. b) MS ion currents for methanol (red squares, m/z = 31), ethylene (orange circles, m/z = 27), higher alkenes (green triangles, m/z = 41) and aromatics (magenta diamond, m/z = 91), measured at TOS corresponding to the UV-Raman spectra reported above.

The operando UV-Raman data of MTH over the Beta catalysts are reported in Figure 3a. In comparison to ZSM-5, Beta exhibits generally broader signals (particularly at longer TOS), compatible with the formation of a bulkier type of coke. Most of the molecular species are clearly evident only in the first spectrum of the set, where some sharp features are observed in the low frequency region. The main contribution is the 1350 cm^{-1} peak, which is ascribed to

phenanthrene. Its intensity readily decreases with TOS, which allows to distinguish the band of naphthalene at 1380 cm^{-1}, after about one hour. A similar evolution is observed for the 1225 cm^{-1} peak, which falls into the region of polymethylated benzenes. Both molecules are reacting further: while phenanthrene is expected to develop into bulk carbon, the PMBs probably first condense into PAHs.

Concerning the extended carbon phase, the position of the G band and the modulation of the background at frequencies close to the ones of the D and the T bands suggest it is again an amorphous carbon with a significant content of sp^3 centres. Only in the first spectrum, the G band looks slightly extended toward higher frequencies, probably as a consequence of the overlap of the most intense bands of heathen and naphthalene (1600 cm^{-1} and 1630 cm^{-1} respectively). PAHs are progressively converted toward bulk as TOS increases, as demonstrated by the progressive reduction of their Raman signals with time. This behaviour is compatible with the high maximum kinetic diameter for species which can diffuse outside of the pores network of this topology (see Table 1), allowing small PAHs observed at early TOS to migrate toward the external surface and to contribute to the building up of bulk coke. This behaviour can be facilitated in this specific sample also because of its smaller particle size (see Table S1), indeed the average length of micropores is shortened and diffusion occurs easier.

Similar to ZSM-5, the MS data reported in Figure 2b (see Figure S3b for the whole MS chart) show that Beta is still close to 100% methanol conversion after the first hour of reaction. However, a slight decrease in the products signals is observed at increasing TOS, in agreement with the shorter lifetime expected (compared to ZSM-5 and SAPO-34, which exhibit about doubled $t_{0.5}$) for this topology.

3.3. Mordenite

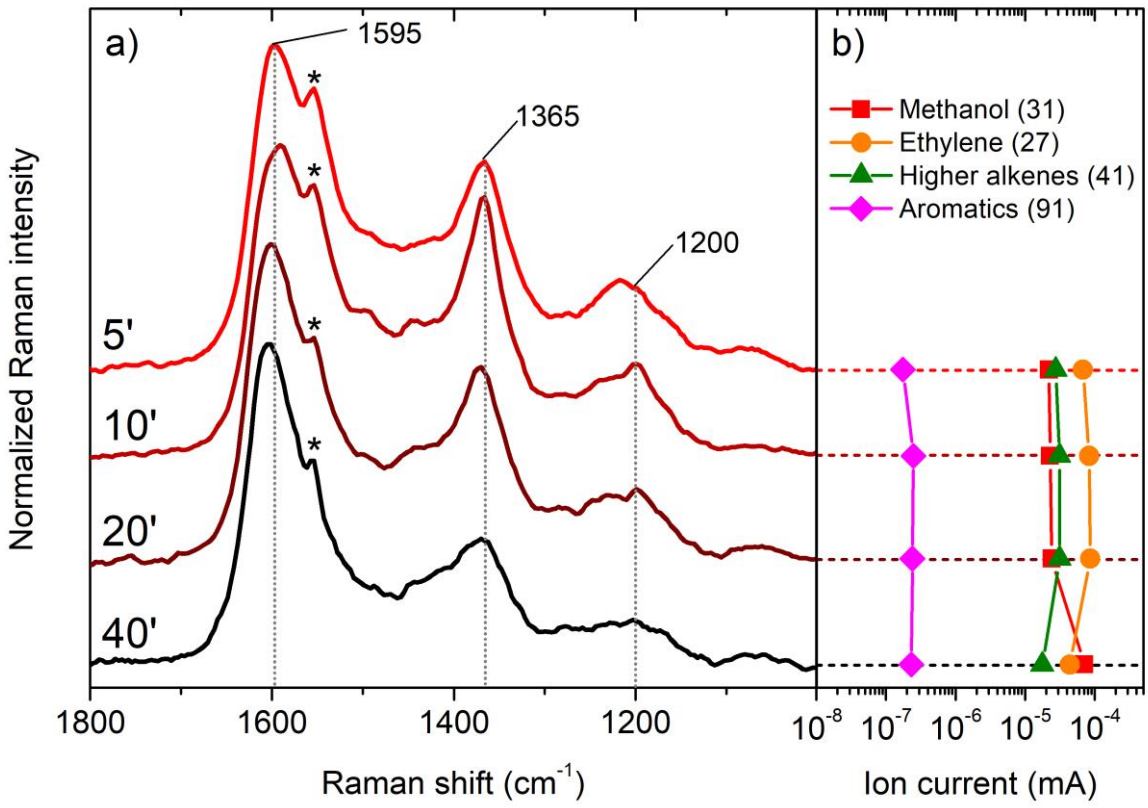

Figure 4. a) UV-Raman spectra of Mordenite collected at different TOS during the MTH reaction (400 °C, WHSV = 2 $g_{MeOH}\ g_{cat}^{-1}\ h^{-1}$). The asterisk (*) labels the contribution associated to atmospheric O_2. b) MS ion currents for methanol (red squares, m/z = 31), ethylene (orange circles, m/z = 27), higher alkenes (green triangles, m/z = 41) and aromatics (magenta diamond, m/z = 91), measured at TOS corresponding to the UV-Raman spectra reported above.

From the whole set of catalysts, Mordenite was deactivating the fastest. Also in this case, the (few) molecular fingerprints overlap with a bulk carbon background (UV-Raman spectra are reported in Figure **4**).

The main molecular feature is a very sharp band centred at 1365 cm^{-1}, which increases in intensity during the early reaction stages and then rapidly loses intensity at longer TOS. Among

the available references, none exactly matches this frequency. The mode falls exactly between two major features of naphthalene (1380 cm^{-1}) and phenanthrene (1350 cm^{-1}): the presence of the latter is further confirmed by the small shoulder at 1450 cm^{-1}. We therefore propose that the 1365 cm^{-1} band could results from the convolution of the signals of these two molecules. The methylation of naphthalene and phenantrene may originate signals in that spectral region too (see Figure S2). The broad and structured band at around 1200 cm^{-1} follows a similar time evolution as the 1365 cm^{-1} feature, indicating that it is related to the same methylated PAHs.

The observed time evolution is particularly interesting, since the short lifetime of this catalyst (as expected by its short $t_{0.5}$ and its high value of a, see Table S2) allowed to follow the speciation until complete deactivation. An interesting picture arises from the combination of the UV-Raman spectra (Figure 3a) with the corresponding activity data (MS signals in Figure 3b, full charts in Figure S3c): as long as methanol is fully converted (i.e. until its MS signals starts to increase at TOS among 10-20 min), the Raman signals associated to molecular coke species grow with respect to the bulk carbon features. As soon as the MS signal of methanol begins to rise (i.e. its conversion drops), the ratio between molecular and bulk coke seems to be reverted. On the basis of these observations, we conclude that for Mordenite deactivation occurs when small PAHs start to condense into bulk carbon. This carbon growth reaction is apparently favoured when the methanol accessibility to active sites decreases and therefore further accelerates the deactivation. Since the extended carbon structures can only form on the external surface, it is likely that the PAHs are able to diffuse out from the large 12-rings in MOR, in agreement with the similar observations for the wide-pores beta zeolite.

3.4. ZSM-22

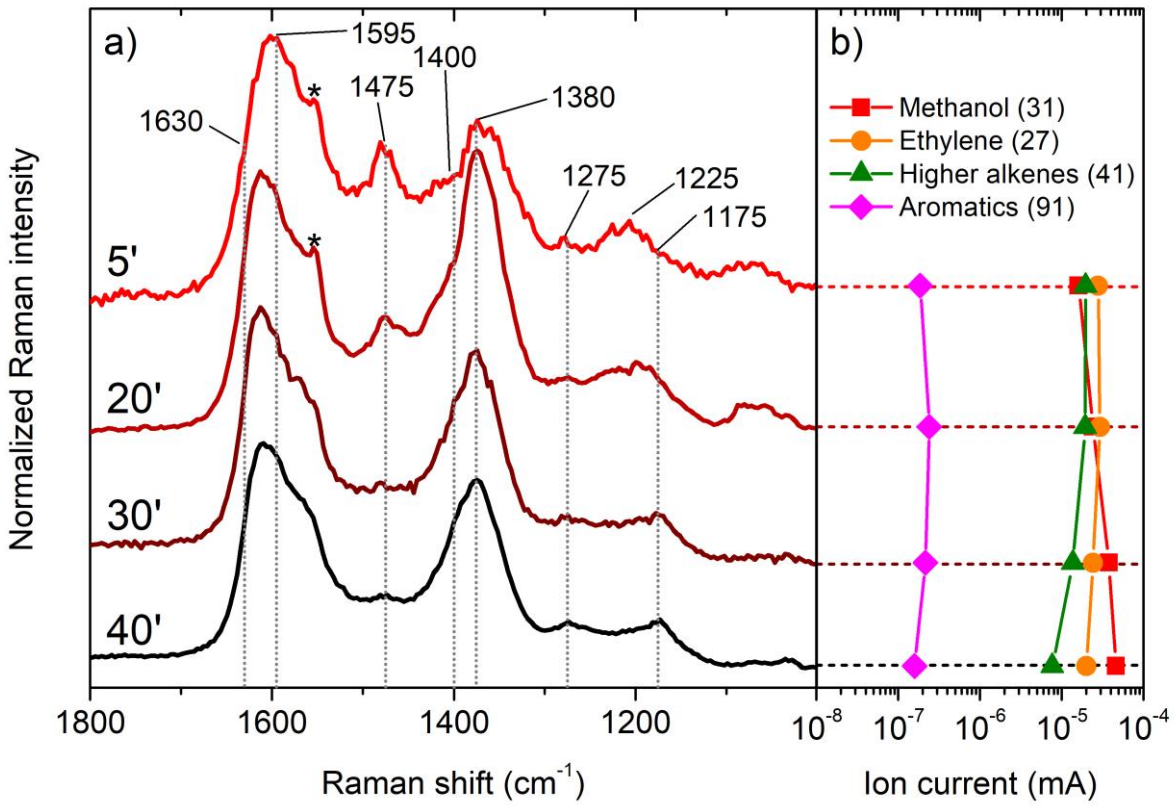

Figure 5. a) UV-Raman spectra of ZSM-22 collected at different TOS during the MTH reaction (400 °C, WHSV = 2 g_{MeOH} g_{cat}^{-1} h^{-1}). The asterisk (*) labels the contribution associated to atmospheric O_2. b) MS ion currents for methanol (red squares, m/z = 31), ethylene (orange circles, m/z = 27), higher alkenes (green triangles, m/z = 41) and aromatics (magenta diamond, m/z = 91), measured at TOS corresponding to the UV-Raman spectra reported above.

Compared to the previously described topologies, the Raman spectra for ZSM-22 (Figure **5**a) are markedly different. In particular, in the beginning the spectra are rich in peaks and shoulders, which relates to specific molecular species.

A peculiar evolution of the 1600 cm^{-1} band is observed: after 5' of reaction the maximum of the band is placed at 1595 cm^{-1}, testifying the presence of amorphous carbon. At increasing TOS,

the maximum of the band shifts to higher frequencies and the growth of a shoulder at around 1630 cm^{-1} becomes evident indicating the build-up of PAHs. This is further confirmed by the increase of intensity around 1400 cm^{-1}: this band turns to be predominant after 20', showing a sharp peak at 1380 cm^{-1}. The latter is related to naphthalene formation. The asymmetric profile of the band towards higher wavenumbers and the subsequent evolution of the shoulder at 1400 cm^{-1} with increasing TOS is interpreted as a successive conversion of naphthalene into anthracene.

The sharp peak centred at 1475 cm^{-1}, which progressively disappears proceeding with the reaction, represents a peculiar feature of this sample. It can be assigned to fluorene, even if its main fingerprint falls below the 1600 cm^{-1} band and thus is not easily identifiable.

A feature with rather constant intensity is observed at 1275 cm^{-1}, which coincides with the main signal of tetramethylbenzene. The fact that this band is not affected by the decreasing conversion (Figure 4b), indicates that tetramethylbenzene is not a very active HC-pool species in ZSM-22.

Finally, some time evolution is observed at lower frequencies, where a sharp band emerges at 1175 cm^{-1} from the broad signal observed at short reaction times: this most probably relates to methylated PAHs forming upon the conversion of naphthalene to bulkier byproducts.

The MS signal of methanol increases only slightly during the first 20-30 min, while the signals of products stay stable during this time (Figure 4b, full chart in Figure S3d). After this initial period, the methanol slope increases more rapidly coinciding with the growth of the Raman features of anthracene. The rather high deactivation rate (lower only to Mordenite) is fully compatible with the catalytic performance descriptors for this sample (see Table S2). This observation suggests as anthracene might be the endpoint of the deactivation process in ZSM-22,

thereby ascribable to a molecular type of coke. This assumption is fully compatible with the low kinetic diameters for diffusion/inclusion proper of this topology (see Table 1).

3.5. SAPO-34

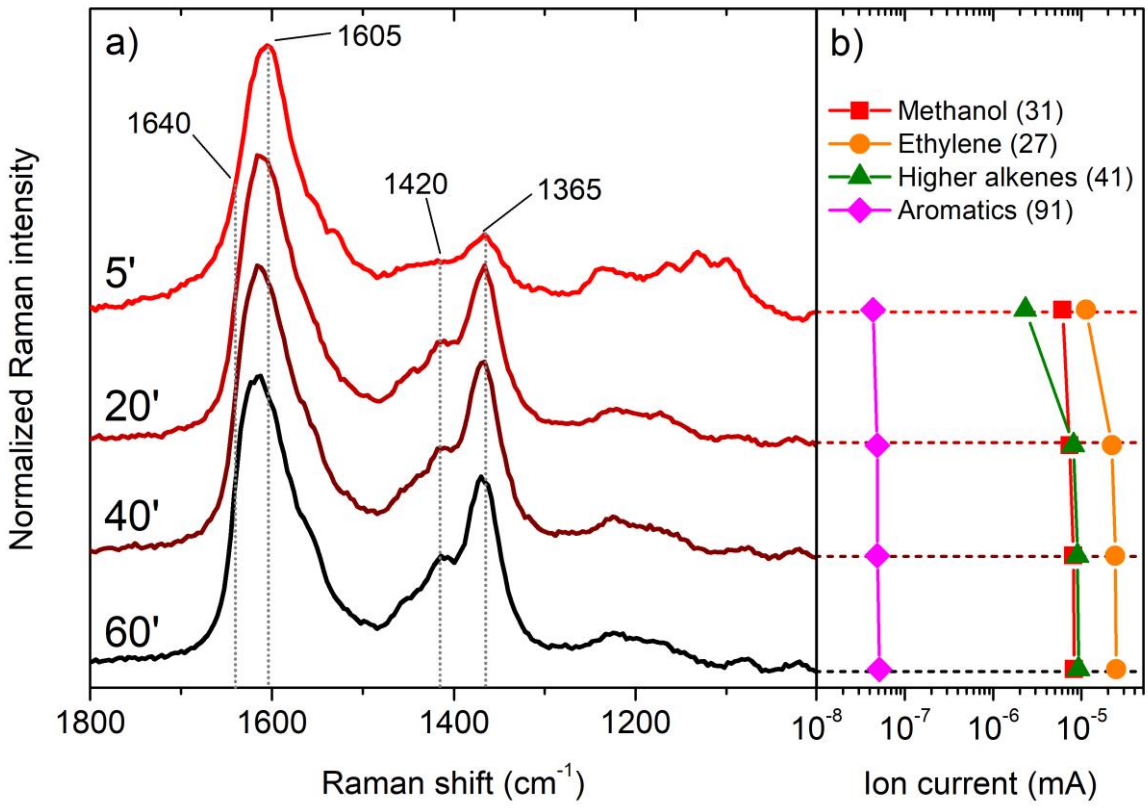

Figure 6. a) UV-Raman spectra of SAPO-34 collected at different TOS during the MTH reaction (400 °C, WHSV = 2 g_{MeOH} g_{cat}^{-1} h^{-1}). The asterisk (*) labels the contribution associated to atmospheric O_2. b) MS ion currents for methanol (red squares, m/z = 31), ethylene (orange circles, m/z = 27), higher alkenes (green triangles, m/z = 41) and aromatics (magenta diamond, m/z = 91), measured at TOS corresponding to the UV-Raman spectra reported above.

As for ZSM-22, the set of Raman spectra for SAPO-34 (Figure 6a) are more typical for molecular type of carbon species. However, from the earliest stages of the reaction, the spectra are dominated by the feature by a band at 1605 cm^{-1}, which is probably related to some external bulk coke deposition. As the TOS increases, the maximum shifts to higher wavenumbers, suggesting the growth of new components at high frequencies. In particular, the peak shows a

shoulder at about 1640 cm^{-1}: this peculiarly high shift value is no longer ascribable to aromatic species, and thus needs to be attributed to alkenes.[62] Also considering the growing intensity of the peak at 1420 cm^{-1}, this feature can be associated to the formation of terminal and/or branched olefins such as isobutene (as a representative example, see the spectrum of 1-hexene in Figure S1b).

However, most striking for SAPO-34 is the fast growing signal with a sharp maximum at 1365 cm^{-1}: as commented for Mordenite, this signal is not directly assignable to the available reference compound, but it should be related to methylated PAHs (also found in dissolution-extraction experiments).[8] The MS data for SAPO-34 shows almost full methanol conversion right from the start of the reaction (in line with its high productivity and long lifetime, see Table S2), while the followed products ethylene and higher alkenes reach a plateau first after 20 min of reaction (Figure 5b, full chart in Figure S3e). This peculiar behaviour has been reported and related to the size of the SAPO-34 crystals, especially observed when these are large.[63] Combining the spectral and the activity data strongly suggests that methylated PAHs, in particular methylated naphthalenes slowly build up and become active (and selective) hydrocarbon pool species in SAPO-34.

3.6. Overall comparison

Even if different reaction stages are probed, the *operando* UV-Raman data allow to depict some common reactivity trends for hydrocarbon species in the five different zeolites, at least at early reaction stages. The topology of each catalyst becomes predominant at later TOS, where the peculiar features of the porous networks drive the reactivity of hydrocarbons through peculiar routes. The short lifetime observed for Mordenite and ZSM-22 allowed to obtain a quite direct

correlation between hydrocarbon species and deactivation pathway. ZSM-5 and SAPO-34 exhibited the longest lifetimes (see also Table S2); hence, only the initial stages, up to the reaching of the steady-state conversion, have been investigated during the first hour of reaction. Therefore, the obtained data provide valuable information on the formation of the active hydrocarbon pool species. Beta showed an intermediate behaviour, since methanol conversion was clearly decreasing at the longer TOS, but the deactivation process was still in progress. The key assignments from Raman and their time evolution for each catalyst are outlined in Table 2.

Table 2. Main vibrational fingerprints observed in the UV-Raman experiments and their assignments to deactivating species for a specific catalyst topology. A raw overview on time evolution is given considering early vs. late reaction stages species.

Frequency	Assignment	ref	Early stages	Late stages
1640	Olefins	tw	-	SAPO-34
1630	Naphthalene Anthracene Phenanthrene	29	-	ZSM-22, ZSM-5
1605-1590	G-band, bulk amorphous carbon (sp^2), Fluorene	23	All	ZSM-5, Beta, Mordenite
1475	Fluorene	tw	ZSM-22	-
1420	Methylated PAHs	tw	-	ZSM-5, SAPO-34
1400	Anthracene	29	-	ZSM-22
1380	Naphthalene	29	ZSM-5, Beta, ZSM-22, Mordenite,	ZSM-5, Beta,
1365	Methylated PAHs	tw	Mordenite, SAPO-34	SAPO-34
1350	Phenanthrene	30	ZSM-5, Beta, Mordenite,	
1280-1275	Methylated benzenes	tw, 43-47		ZSM-5, ZSM-22
1200-1175	Methylated PAHs	tw	Mordenite	ZSM-5, ZSM-

		22		
1100-1000	T-band, bulk amorphous carbon (sp^3)	23	Beta, Mordenite	ZSM-5, Beta, Mordenite

Interestingly, for the reaction conditions adopted in this work (*i.e.* quasi-CSTR conditions), all catalysts develop similar molecular species, though at very different reaction stages. In particular, naphthalene and phenanthrene, eventually in their methylated forms, are encountered in the whole set of catalysts. However, in the fast deactivating topologies, these species represent either the last step of a series of organic transformations, (i.e. anthracene in the case of ZSM-22) or the next-to-last step to give heavier products (i.e. bulk carbon in the case of Mordenite). In both cases the topology seems to be directly related to the shape and/or size of the deactivating species. Other important species encountered in most of the topologies are methylated benzenes (MBs), which generally have been considered to be the active species in the aromatic-based cycle of the hydrocarbon pool mechanism.[6] The *operando* UV-Raman data clearly confirm the dominating role of MBs for the active hydrocarbon pool in the case of ZSM-5, while in ZSM-22 they seem to be more a spectator species. Also in the case of SAPO-34, several earlier works provided evidence for the role of MBs as active hydrocarbon pool species. However, we have shown here that methylated naphthalenes are potentially part of the active the hydrocarbon pool species. This finding is in agreement with previous ex-situ work based on ^{13}C-methanol labelling experiments.[64, 65] Finally, for BEA topology, the fast decrease of molecular species followed by the steady increase of extended carbon structures indicates a very different deactivation pathway. The concomitant slow decrease in activity is in agreement with a deactivation mechanism characterized by pore blocking, rather than by direct active site blocking. A schematic overview of the different hydrocarbon transformation steps is given in Figure 6.

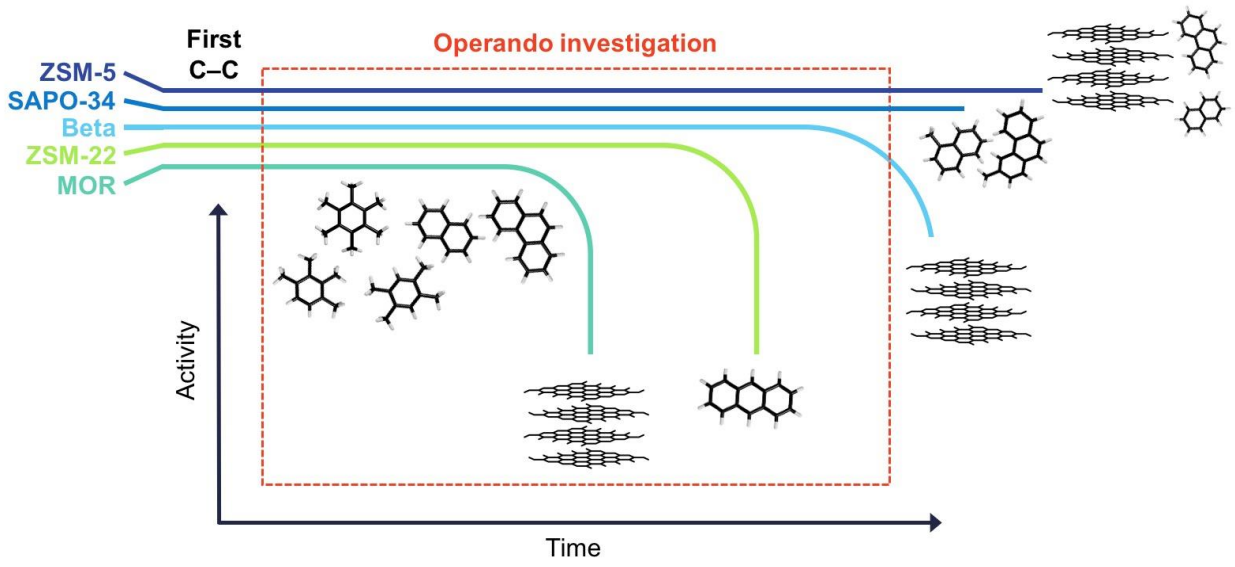

Figure 7. Schematic representation of the key species identified in this study. At short lifetimes common chemical species are identified for all the topologies, while these evolve toward different ones at increasing TOS. For short-living catalysts (i.e. Mordenite and ZSM-22), the latter are most probably the prevalent deactivating species, whereas are still evolving (and possibly taking part to the reaction) in long-living zeolites.

4. Conclusions

This work reports a thorough operando spectroscopic investigation of five different zeolite topologies during the catalytic conversion of methanol to hydrocarbons. The topology of each catalyst provides different transport properties for the reacting hydrocarbon molecules leading to markedly different reaction pathways. The wide porosity of Beta and Mordenite favours diffusion of rather bulky molecules, which progressively grow until they are converted into bulk coke while approaching deactivation. The case of Mordenite clearly exemplifies this scenario: PAHs accumulate until methanol is properly supplied to the active sites, then they begin to react toward carbon as soon as the reactant becomes scarce in the reaction environment. Despite the very different topologies, ZSM-22 and SAPO-34 appear to deactivate both via the accumulation

of molecular coke, in a “ship in the bottle” fashion. Since ZSM-22 exhibits a short lifetime, the molecular endpoint of its deactivation path has been identified as anthracene, which represents a perfect tamping molecule for the one dimensional 10-ring channels. For SAPO-34, methanol breakthrough and complete deactivation did not occur in the time of the investigation, but the lack of signals for the growth of extended carbon structures suggests that naphthalenes are participating in the active hydrocarbon pool until they eventually exceed the available space provided by the large CHA cages. ZSM-5 shows an intermediate behaviour: while PMBs are participating in the active hydrocarbon pool and form part of the product stream, bulk coke grows in parallel, but the three-dimensional pore structure allows reactants access to and from the active sites.

Clearly, the analysis of the Raman spectra has been challenging, but we believe that the application of advanced operando methods is mandatory for obtaining further insights on the complex MTH chemistry. In particular, we found that in the commercially relevant SAPO-34, small polycyclic aromatics hydrocarbons (PAHs) form part of the active hydrocarbon pool, whereas these molecules have usually been considered as stable and mostly deactivating species. The last point represents the first experimental evidence of such behaviour reported in the literature, highlighting the importance of advanced operando approaches. In the future the UV-Raman method could be combined, maybe even simultaneously, with additional operando characterization techniques, such as UV-vis and FTIR spectroscopy or X-Ray diffraction.

Electronic Supplementary information (ESI)

Electronic Supplementary Information (ESI) available: UV-Raman spectra of some reference compounds (Figure S1); calculated Raman spectra of some methylated PAHs (Figure S2) with related computational details; full MS charts collected during operando experiments (figure S3).

Corresponding Authors

* Matteo Signorile, matteo.signorile@unito.it

* Pablo Beato, pabb@topsoe.com

Conflicts of interest

There are no conflicts to declare.

Acknowledgments

This work is part of the MS and DRG PhD theses. This publication is part of the European Industrial Doctorate Project "ZeoMorph" (Grant Agreement No. 606965). The financial support from the European Research Council via Marie Curie Actions (FP7- PEOPLE-2013-ITN-EID) is acknowledged. Dr. Anna M. Lind and Dr. Bjørnar Arstad at SINTEF Materials and Chemistry are kindly acknowledged for preparing the SAPO-34 catalyst. Modelling was performed on the Abel Cluster, in the framework of the N9381K and NN4683K NOTUR grants. MS, FB and SB acknowledge Open Access Labs project for funding (2013-2015 agreement of Compagnia di San Paolo and Università di Torino).

References

1. M. Stöcker, *Microporous and Mesoporous Materials*, 1999, **29**, 3-48.
2. U. Olsbye, S. Svelle, M. Bjørgen, P. Beato, T. V. W. Janssens, F. Joensen, S. Bordiga and K. P. Lillerud, *Angewandte Chemie International Edition*, 2012, **51**, 5810-5831.

3. B. Smit and T. L. M. Maesen, *Nature*, 2008, **451**, 671-678.
4. S. M. Csicsery, *Zeolites*, 1984, **4**, 202-213.
5. P. B. Venuto, *Microporous Materials*, 1994, **2**, 297-411.
6. U. Olsbye, S. Svelle, K. P. Lillerud, Z. H. Wei, Y. Y. Chen, J. F. Li, J. G. Wang and W. B. Fan, *Chemical Society reviews*, 2015, **44**, 7155-7176.
7. D. Rojo-Gama, S. Etemadi, E. Kirby, K. P. Lillerud, P. Beato, S. Svelle and U. Olsbye, *Faraday Discussions*, 2017, **197**, 421-446.
8. D. Rojo-Gama, M. Signorile, F. Bonino, S. Bordiga, U. Olsbye, K. P. Lillerud, P. Beato and S. Svelle, *Journal of Catalysis*, 2017, **351**, 33-48.
9. F. L. Bleken, K. Barbera, F. Bonino, U. Olsbye, K. P. Lillerud, S. Bordiga, P. Beato, T. V. W. Janssens and S. Svelle, *Journal of Catalysis*, 2013, **307**, 62-73.
10. S. Teketel, W. Skistad, S. Benard, U. Olsbye, K. P. Lillerud, P. Beato and S. Svelle, *ACS Catalysis*, 2012, **2**, 26-37.
11. F. Bleken, W. Skistad, K. Barbera, M. Kustova, S. Bordiga, P. Beato, K. P. Lillerud, S. Svelle and U. Olsbye, *Physical Chemistry Chemical Physics*, 2011, **13**, 2539-2549.
12. H. Schulz, *Catalysis Today*, 2010, **154**, 183-194.
13. M. Westgård Erichsen, S. Svelle and U. Olsbye, *Catalysis Today*, 2013, **215**, 216-223.
14. K. Barbera, F. Bonino, S. Bordiga, T. V. W. Janssens and P. Beato, *Journal of Catalysis*, 2011, **280**, 196-205.
15. I. Yarulina, J. Goetze, C. Gucuyener, L. van Thiel, A. Dikhtiarenko, J. Ruiz-Martinez, B. M. Weckhuysen, J. Gascon and F. Kapteijn, *Catal Sci Technol*, 2016, **6**, 2663-2678.
16. D. S. Wragg, M. G. O'Brien, F. L. Bleken, M. Di Michiel, U. Olsbye and H. Fjellvag, *Angewandte Chemie International Edition*, 2012, **51**, 7956-7959.
17. P. del Campo, W. A. Slawinski, R. Henry, M. W. Erichsen, S. Svelle, P. Beato, D. Wragg and U. Olsbye, *Surface Science*, 2016, **648**, 141-149.
18. J. Goetze, F. Meirer, I. Yarulina, J. Gascon, F. Kapteijn, J. Ruiz-Martínez and B. M. Weckhuysen, *ACS Catalysis*, 2017, **7**, 4033-4046.
19. Q. Qian, C. Vogt, M. Mokhtar, A. M. Asiri, S. A. Al-Thabaiti, S. N. Basahel, J. Ruiz-Martínez and B. M. Weckhuysen, *ChemCatChem*, 2014, **6**, 3396-3408.
20. J. W. Park and G. Seo, *Applied Catalysis A: General*, 2009, **356**, 180-188.

21. R. F. Howe, E. K. Gibson, C. R. A. Catlow, A. Hameed, J. McGregor, P. Collier, S. F. Parker and D. Lennon, *Faraday Discussions*, 2017, **197**, 447-471.
22. A. C. Ferrari and J. Robertson, *Physical Review B*, 2000, **61**, 14095-14107.
23. A. C. Ferrari and J. Robertson, *Physical Review B*, 2001, **64**, 075414.
24. A. C. Ferrari, J. Meyer, V. Scardaci, C. Casiraghi, M. Lazzeri, F. Mauri, S. Piscanec, D. Jiang, K. Novoselov and S. Roth, *Physical Review Letters*, 2006, **97**, 187401.
25. M. S. Dresselhaus, G. Dresselhaus, R. Saito and A. Jorio, *Physics Reports*, 2005, **409**, 47-99.
26. J. Ferguson, L. W. Reeves and W. G. Schneider, *Can. J. Chem.*, 1957, **35**, 1117-1136.
27. J. Catalan and J. Carlos Del Valle, *J. Phys. Chem. B*, 2014, **118**, 5168-5176.
28. E. Borodina, F. Meirer, I. Lezcano-González, M. Mokhtar, A. M. Asiri, S. A. Al-Thabaiti, S. N. Basahel, J. Ruiz-Martinez and B. M. Weckhuysen, *Acs Catalysis*, 2015, **5**, 992-1003.
29. M. Signorile, F. Bonino, A. Damin and S. Bordiga, *The Journal of Physical Chemistry C*, 2015, **119**, 11694-11698.
30. Y. T. Chua and P. C. Stair, *Journal of Catalysis*, 2003, **213**, 39-46.
31. J. Li, G. Xiong, Z. Feng, Z. Liu, Q. Xin and C. Li, *Microporous and Mesoporous Materials*, 2000, **39**, 275-280.
32. C. Li and P. C. Stair, *Catalysis Today*, 1997, **33**, 353-360.
33. P. Beato, E. Schachtl, K. Barbera, F. Bonino and S. Bordiga, *Catalysis Today*, 2013, **205**, 128-133.
34. M. Signorile, F. Bonino, A. Damin and S. Bordiga, *Topics in Catalysis*, 2018, DOI: 10.1007/s11244-018-1033-z.
35. H. An, F. Zhang, Z. Guan, X. Liu, F. Fan and C. Li, *ACS Catalysis*, 2018, DOI: 10.1021/acscatal.8b00928.
36. W. Skistad, PhD dissertation PhD dissertation, University of Oslo, 2014.
37. M. Signorile, PhD dissertation PhD dissertation, Università di Torino, 2017.
38. D. Rojo-Gama, PhD dissertation PhD dissertation, University of Oslo, 2017.
39. D. Rojo-Gama, L. Mentel, G. N. Kalantzopoulos, D. K. Pappas, I. Dovgaliuk, U. Olsbye, K. P. Lillerud, P. Beato, L. F. Lundegaard, D. S. Wragg and S. Svelle, *Journal of Physical Chemistry Letters*, 2018, **9**, 1324-1328.

40. D. Rojo-Gama, M. Nielsen, D. S. Wragg, M. Dyballa, J. Holzinger, H. Falsig, L. F. Lundegaard, P. Beato, R. Y. Brogaard, K. P. Lillerud, U. Olsbye and S. Svelle, *ACS Catalysis*, 2017, **7**, 8235-8246.
41. J. F. Haw and D. M. Marcus, *Topics in Catalysis*, 2005, **34**, 41-48.
42. S. Müller, Y. Liu, M. Vishnuvarthan, X. Sun, A. C. van Veen, G. L. Haller, M. Sanchez-Sanchez and J. A. Lercher, *Journal of Catalysis*, 2015, **325**, 48-59.
43. P. del Campo, U. Olsbye, K. P. Lillerud, S. Svelle and P. Beato, *Catalysis Today*, 2018, **299**, 135-145.
44. J. Kim, M. Choi and R. Ryoo, *Journal of Catalysis*, 2010, **269**, 219-228.
45. M. Milina, S. Mitchell, P. Crivelli, D. Cooke and J. Perez-Ramirez, *Nat. Commun.*, 2014, **5**.
46. A. Molino, K. A. Lukaszuk, D. Rojo-Gama, K. P. Lillerud, U. Olsbye, S. Bordiga, S. Svelle and P. Beato, *Chem. Commun.*, 2017, **53**.
47. S. Teketel, L. F. Lundegaard, W. Skistad, S. M. Chavan, U. Olsbye, K. P. Lillerud, P. Beato and S. Svelle, *Journal of Catalysis*, 2015, **327**, 22-32.
48. http://www.iza-structure.org/).
49. T. V. W. Janssens, *Journal of Catalysis*, 2009, **264**, 130-137.
50. D. A. Long, *The Raman effect*, John Wiley & Sons, Ltd, Chichester, UK, 2002.
51. F. Márquez, C. M. Zicovich-Wilson, A. Corma, E. Palomares and H. García, *The Journal of Physical Chemistry B*, 2001, **105**, 9973-9979.
52. S. A. Asher, *Anal. Chem.*, 1993, **65**, 59-66.
53. M. Bjorgen, F. Bonino, B. Arstad, S. Kolboe, K. P. Lillerud, A. Zecchina and S. Bordiga, *Chemphyschem*, 2005, **6**, 232-235.
54. M. Bjorgen, F. Bonino, S. Kolboe, K. P. Lillerud, A. Zecchina and S. Bordiga, *J. Am. Chem. Soc.*, 2003, **125**, 15863-15868.
55. M. Signorile, F. Bonino, A. Damin and S. Bordiga, *The Journal of Physical Chemistry C*, 2016, **120**, 18088-18092.
56. W. H. Fletcher and J. S. Rayside, *J. Raman Spectrosc.*, 1974, **2**, 3-14.
57. J. H. S. Green, *Spectrochim. Acta A*, 1970, **26**, 1913-1923.
58. J. H. S. Green, *Spectrochim. Acta A*, 1970, **26**, 1523-1533.
59. J. H. S. Green, *Spectrochim. Acta A*, 1970, **26**, 1503-1513.

60. J. H. S. Green, D. J. Harrison and W. Kynaston, *Spectrochim. Acta A*, 1971, **27**, 807-815.
61. J. H. S. Green, D. J. Harrison and W. Kynaston, *Spectrochim. Acta A*, 1971, **27**, 793-806.
62. N. Sheppard and D. M. Simpson, *Q. Rev. Chem. Soc.*, 1952, **6**.
63. K. Y. Lee, H.-J. Chae, S.-Y. Jeong and G. Seo, *Applied Catalysis A: General*, 2009, **369**, 60-66.
64. M. Bjorgen, S. Akyalcin, U. Olsbye, S. Benard, S. Kolboe and S. Svelle, *Journal of Catalysis*, 2010, **275**, 170-180.
65. W. G. Song, H. Fu and J. F. Haw, *J. Phys. Chem. B*, 2001, **105**, 12839-12843.